

WIMP Meets ALP: Coherent Freeze-Out of Dark Matter

Steven Ferrante,^{*} Maxim Perelstein,[†] and Bingrong Yu[‡]

Department of Physics, LEPP, Cornell University, Ithaca, NY 14853, USA

We consider the cosmological history of a weakly interacting massive particle (WIMP) coupled to a light axion-like particle (ALP) via a quadratic coupling. Although the coupling is too feeble to thermalize the ALP, coherent forward scattering between the two sectors induces temperature-dependent mass shifts that substantially modify both WIMP freeze-out and ALP misalignment dynamics, giving rise to a novel *coherent freeze-out* mechanism. At high temperatures, the WIMP thermal bath spontaneously breaks the symmetry of the ALP potential, displacing the field to a new vacuum. The resulting back-reaction reduces the WIMP effective mass and delays its freeze-out. Depending on the strength of the coupling, symmetry restoration occurs via either a first-order phase transition (FOPT) or a crossover. In the FOPT regime, dark matter consists solely of WIMPs, whose delayed freeze-out permits annihilation cross sections up to two (five) orders of magnitude above the standard value for s -wave (p -wave) annihilation, while still yielding the correct relic density. In the crossover regime, both WIMP and ALP can contribute to dark matter. Remarkably, we find an “ALP miracle”: a Planck-suppressed quadratic coupling yields an ALP abundance comparable to the observed dark matter density, largely independent of its initial displacement and mass.

I. INTRODUCTION

The particle nature of dark matter (DM) remains unknown. Two well-motivated candidates beyond the Standard Model (SM) are weakly interacting massive particles (WIMPs) and axion-like particles (ALPs) (see [1, 2] for recent reviews). They inhabit very different mass ranges and arise from distinct theoretical frameworks, and their cosmological production mechanisms likewise differ sharply. WIMPs begin in thermal equilibrium and obtain their relic abundance through freeze-out, a process largely insensitive to ultraviolet (UV) physics. ALPs, by contrast, never thermalize due to their extremely weak couplings; their relic abundance is instead determined by the initial field displacement at the onset of coherent oscillation, typically set by inflationary fluctuations or other high-scale dynamics.

In this work, we raise a generic question: if both a WIMP and an ALP are present in the fundamental Lagrangian, what are the cosmological consequences of an interaction between them? Since the coupling is typically too weak to thermalize the ALP, one might expect their dynamics to remain independent, as no significant momentum exchange occurs. However, this intuition fails. The ALP behaves as a coherent, homogeneous field, while the WIMP population forms an approximately uniform thermal bath. Coherent forward scattering between the two backgrounds induces mean-field corrections to the dispersion relations of both species: the ALP potential is deformed by the thermal WIMP bath, and the WIMP effective mass is shifted by the ALP background. These medium effects lead to coupled, nontrivial dynamics in their cosmological evolution. The goal of this paper is to

show that even an extremely weak (Planck-suppressed) coupling between the two sectors leads to striking cosmological consequences.

To illustrate the mechanism, we consider a simple model in which WIMP and ALP fields interact through an effective quadratic coupling (see Eq. (1)). The thermal bath of WIMPs induces a temperature-dependent correction to the ALP potential, spontaneously breaking its discrete symmetry at high temperatures and restoring it at low temperatures. In the broken phase, the ALP field is displaced to a new vacuum, whose back-reaction reduces the effective WIMP mass and therefore affects its freeze-out. At the same time, ALP coherent oscillations only begin after the phase transition, with the initial value of the field fixed by the high-temperature dynamics, in contrast with the usual misalignment mechanism.

This setup leads to several key consequences: (i) the symmetry restoration of the ALP potential is governed by a single dimensionless parameter, which determines whether the system undergoes a first-order phase transition (FOPT) or a smooth crossover; (ii) in the FOPT regime, the WIMP may remain in thermal equilibrium far longer than in the standard picture, leading to a substantial enhancement of its relic abundance – the scenario we call “coherent freeze-out”; (iii) in the crossover regime, the ALP obtains a relic abundance that deviates from the usual misalignment prediction and, remarkably, is insensitive to both the initial ALP field value and the ALP mass.

Modifications to the dynamics of a light scalar in the presence of a thermal bath have been discussed in several contexts (see, e.g., [3–9]). The crucial distinction in our analysis is that we fully incorporate the back-reaction of the scalar on the thermal bath – an effect that plays a central role in our mechanism, especially in the FOPT regime.

^{*} sef87@cornell.edu

[†] m.perelstein@cornell.edu

[‡] bingrong.yu@cornell.edu

II. DYNAMICS

We begin with the following effective coupling,

$$\mathcal{L}_{\text{eff}} \supset \frac{1}{\Lambda} \bar{\chi} \chi \frac{\phi^2}{2}, \quad (1)$$

where Λ is the cutoff scale, χ is a fermionic WIMP (either Dirac or Majorana), and ϕ is a light real scalar. For convenience, we refer to ϕ as the ALP hereafter, although it may be CP-even or CP-odd. The model contains three hierarchical scales, $\Lambda \gg m_\chi \gg m_\phi$, with m_χ and m_ϕ denoting the physical zero-temperature masses of χ and ϕ , respectively. For simplicity, we do not include higher-order terms in ϕ in the zero-temperature potential. The coupling in (1) is generic and can arise in a wide range of UV completions. We take a definite sign for the interaction, which is essential for our analysis. Scalar-fermion interactions with the same structure as (1), including the sign, appear in familiar contexts. For example, this is the structure of the leading non-derivative interaction between nucleons and pions in the SM, or between nucleons and the QCD axion in minimal extensions, both of which follow directly from chiral effective theory [10–15]. Throughout, we assume the coupling is small enough that ϕ never thermalizes (neither chemically nor kinematically), which requires $\Lambda \gg \sqrt{T_{\text{RH}} M_{\text{Pl}}}$, where T_{RH} is the reheating temperature of the Universe and $M_{\text{Pl}} \approx 1.2 \times 10^{19}$ GeV is the Planck mass.

Even without momentum exchange, coherent forward scattering modifies the propagation of both species. In the region of interest, χ is in thermal equilibrium with the SM. The thermal χ background shifts the ALP mass, and the classical ALP field shifts the WIMP mass,

$$m_{\phi, \text{eff}}^2 = m_\phi^2 - \frac{\langle \bar{\chi} \chi \rangle_T}{\Lambda}, \quad (2)$$

$$m_{\chi, \text{eff}} = \left| m_\chi - \frac{\phi^2}{2\Lambda} \right|, \quad (3)$$

where

$$\langle \bar{\chi} \chi \rangle_T = g_\chi \int \frac{d^3 \mathbf{k}}{(2\pi)^3} \frac{m_{\chi, \text{eff}}}{E_{\mathbf{k}}} f_\chi(\mathbf{k}), \quad (4)$$

is the thermally averaged number density, with $E_{\mathbf{k}} \equiv \sqrt{\mathbf{k}^2 + m_{\chi, \text{eff}}^2}$ and $g_\chi = 4(2)$ if χ is Dirac (Majorana).

Crucially, the correction to m_ϕ depends on $m_{\chi, \text{eff}}$, which itself depends on ϕ ; the dynamics of the two sectors are therefore *coupled*.

For analytic control, we adopt a Maxwell-Boltzmann (MB) distribution, $f_\chi = e^{-E_{\mathbf{k}}/T}$. (A more complete treatment – including quantum-statistical effects and thermal corrections beyond quadratic order – can be implemented numerically; see Appendix D. These refinements do not modify the qualitative results.) This leads to the ALP potential

$$V(\phi, T) = \frac{g_\chi}{2\pi^2} m_\chi^4 \mathcal{V}(\varphi, x), \quad (5)$$

with the normalized potential

$$\mathcal{V}(\varphi, x) = -\frac{\varphi^2}{2} \frac{\gamma^2 K_1(\gamma x)}{x} + \kappa \frac{\varphi^2}{2}, \quad (6)$$

where K_1 is the modified Bessel function. Here we have defined $x \equiv m_\chi/T$, the normalized ALP field $\varphi \equiv \phi/\sqrt{m_\chi \Lambda}$, the boost factor $\gamma \equiv |1 - \varphi^2/2|$, and a dimensionless parameter

$$\kappa \equiv \frac{2\pi^2}{g_\chi} \frac{m_\phi^2 \Lambda}{m_\chi^3}. \quad (7)$$

The first term in (6) encodes the thermal effect of the WIMP bath, while the second is the bare ALP mass. The resulting potential, shown in the left panel of Fig. 1, contains a term quartic in φ due to the back-reaction on $m_{\chi, \text{eff}}$, ensuring it is bounded from below. At early times ($\gamma x \ll 1$), the thermal term acts like a negative T^2 mass and spontaneously breaks the Z_2 symmetry ($\phi \rightarrow -\phi$); at late times, the bare mass dominates and restores it. The order of this transition is set by a critical coupling $\kappa_c \approx 0.27$, which can be calculated in Ginzburg-Landau theory (see Appendix A). For $\kappa < \kappa_c$, the transition is first-order, and for $\kappa > \kappa_c$ it is a crossover. We truncate the potential at $|\varphi| = \sqrt{2}$, where $m_{\chi, \text{eff}} \rightarrow 0$ and higher-order terms become important (see Appendix D). Since the field starts with negligible velocity after inflation, $|\dot{\varphi}|$ never exceeds this bound.

In the radiation era, the ALP field obeys the following equation of motion (EOM):

$$\varphi'' + \frac{2}{x} \varphi' - \eta x \left(1 - \frac{\varphi^2}{2}\right) \left[(1 - \varphi^2) K_1(\gamma x) + \frac{\varphi^2}{2} \gamma x K_0(\gamma x) \right] \varphi + \eta \kappa x^2 \varphi = 0, \quad (8)$$

where prime denotes the derivative with respect to x and

$$\eta \equiv \frac{g_\chi}{2\pi^2} \frac{1}{1.66^2 g_*} \frac{M_{\text{Pl}}^2}{m_\chi \Lambda}, \quad (9)$$

with g_* the number of relativistic degrees of freedom. The EOM (8) contains only two free parameters (κ and η), and its solutions are studied in detail in Appendix B.

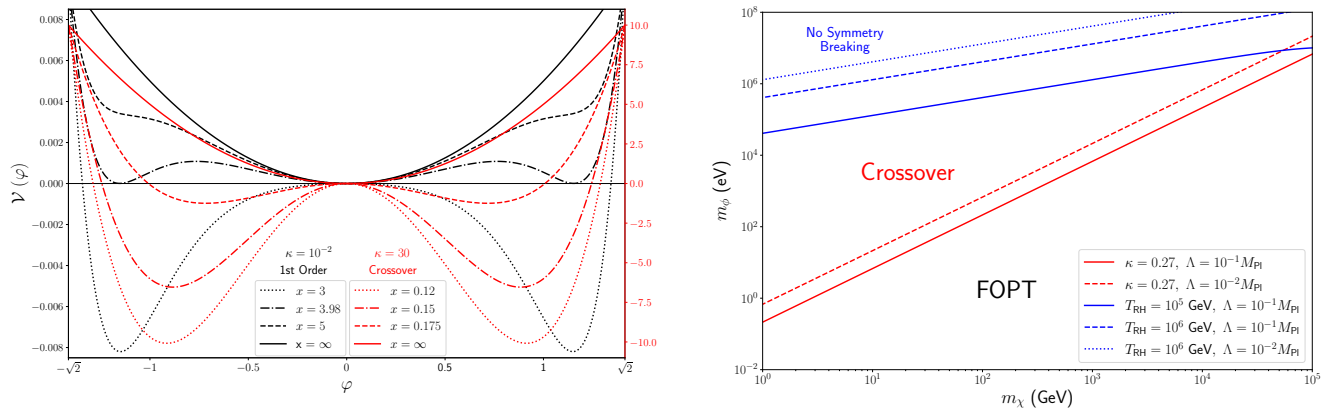


FIG. 1. **Left:** The normalized ALP potential (6) in a thermal bath of WIMPs at several temperatures. For $\kappa \gtrsim 0.27$ the phase transition is first order (black curves), while for $\kappa \lesssim 0.27$ it becomes a crossover (red curves). **Right:** Phase diagram in the (m_χ, m_ϕ) plane. Below the $\kappa = 0.27$ contour (red lines), symmetry restoration proceeds through a first-order phase transition; above it, the transition is a crossover. Symmetry restoration further requires that the symmetry be broken at the onset of radiation domination, T_{RH} . The condition $\kappa = K_1(x_{\text{RH}})/x_{\text{RH}}$ (blue curves), with $x_{\text{RH}} \equiv m_\chi/T_{\text{RH}}$, marks the boundary above which the symmetry is never broken and no transition occurs.

Depending on κ , the resulting parameter space falls into three classes (see right panel of Fig. 1):

1. **No symmetry breaking:** $\kappa > K_1(x_{\text{RH}})/x_{\text{RH}}$ with $x_{\text{RH}} \equiv m_\chi/T_{\text{RH}}$. Symmetry is never broken, and the two sectors decouple.
2. **Crossover:** $0.27 < \kappa < K_1(x_{\text{RH}})/x_{\text{RH}}$. Symmetry is broken at high T and restored smoothly at low T .
3. **FOPT:** $\kappa < 0.27$ and $\kappa < K_1(x_{\text{RH}})/x_{\text{RH}}$. Symmetry is broken at high T and restored at low T through a first-order transition.

In what follows, we focus on the latter two scenarios, where the WIMP and ALP exhibit genuinely coupled dynamics.

III. PHENOMENOLOGY

Now we turn to the DM phenomenology in our mechanism and distinguish two regimes. In the FOPT regime ($\kappa \lesssim 0.27$), the ALP behaves as a spectator field and does not contribute to the relic abundance. In the crossover regime ($\kappa \gtrsim 0.27$), the ALP provides a second DM component whose abundance is largely insensitive to its initial field displacement and mass.

A. First-order phase transition regime

At high temperatures, the ALP potential develops a symmetry-breaking minimum $\varphi_* \neq 0$ (see Fig. 1). We

define \tilde{x}_{cfo} as the time when this local minimum disappears:

$$\left. \frac{\partial \mathcal{V}(\varphi, \tilde{x}_{\text{cfo}})}{\partial \varphi} \right|_{\varphi=\varphi_*} = \left. \frac{\partial^2 \mathcal{V}(\varphi, \tilde{x}_{\text{cfo}})}{\partial \varphi^2} \right|_{\varphi=\varphi_*} = 0, \quad (10)$$

which determines both φ_* and \tilde{x}_{cfo} as functions of κ . In the limit of $\kappa \ll 1$ and $x \gg 1$, the symmetry-breaking vacuum evolves as (see Appendix C)

$$\varphi_* = \sqrt{2 \left(1 - \frac{c_1}{x} \right)}, \quad (11)$$

where $c_1 \approx 1.33$ is the root of $c_1 K_0(c_1) = K_1(c_1)$, and \tilde{x}_{cfo} follows the simple scaling

$$\tilde{x}_{\text{cfo}} = c_2 \kappa^{-1/2}, \quad c_2 \approx 0.45. \quad (12)$$

For $x < \tilde{x}_{\text{cfo}}$, the field remains trapped at φ_* . It returns to $\varphi = 0$ only when $x > \max\{\tilde{x}_{\text{cfo}}, x_{\text{osc}}\}$, where $x_{\text{osc}} \sim m_\chi/\sqrt{m_\phi M_{\text{Pl}}}$ marks the onset of ALP oscillations.

We now show how the above dynamics affect WIMP freeze-out. The Boltzmann equation governing the WIMP number density is

$$\dot{n}_\chi + 3Hn_\chi = -\langle \sigma v \rangle_{\text{eff}} (n_\chi^2 - n_{\chi, \text{eq}}^2). \quad (13)$$

The ALP background reduces the WIMP effective mass, modifying both $\langle \sigma v \rangle_{\text{eff}}$ and the equilibrium distribution:

$$n_{\chi, \text{eq}} = \frac{g_\chi}{2\pi^2} m_{\chi, \text{eff}}^2 T K_2(m_{\chi, \text{eff}}/T). \quad (14)$$

When $\varphi = \varphi_*$, Eq. (11) implies

$$m_{\chi, \text{eff}}/T = (1 - \varphi_*^2/2)x = c_1 \approx 1.33. \quad (15)$$

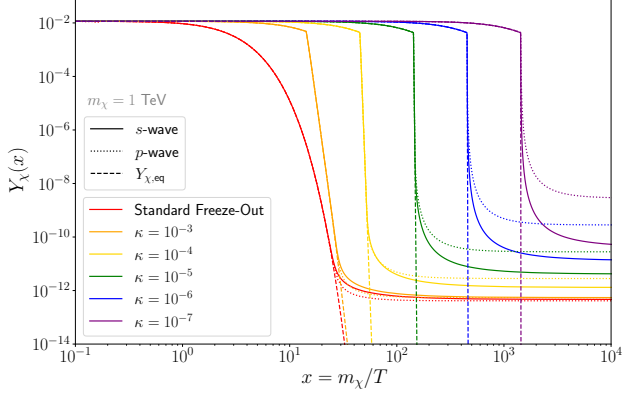


FIG. 2. WIMP yield $Y_\chi \equiv n_\chi/s$ as a function of inverse temperature in the coherent freeze-out scenario. Solid (dotted) curves show the numerical solution of the Boltzmann equation (13) for s -wave (p -wave) annihilation, while dashed curves show the corresponding equilibrium yield (14). For comparison, the standard freeze-out result is shown in red. The benchmark parameters used are $m_\chi = 1$ TeV, with $\sigma_0 = 2.2 \times 10^{-26}$ cm³/s for s -wave and $\sigma_1 = 1.9 \times 10^{-25}$ cm³/s for p -wave domination.

So the argument of the Bessel function remains order unity even at $x \gg 25$. This allows the WIMP to stay in equilibrium far longer than in the standard freeze-out scenario.

Freeze-out is initiated when symmetry is restored. In the parameter space of interest, $\tilde{x}_{\text{cfo}} > x_{\text{osc}}$, so after \tilde{x}_{cfo} , the ALP energy density redshifts as matter, $\varphi(x > \tilde{x}_{\text{cfo}}) = \varphi_*(\tilde{x}_{\text{cfo}}) \times (\tilde{x}_{\text{cfo}}/x)^{3/2}$. This increases the WIMP effective mass:

$$\frac{m_{\chi,\text{eff}}}{m_\chi} = 1 - \frac{\varphi_*^2(\tilde{x}_{\text{cfo}})}{2} \frac{\tilde{x}_{\text{cfo}}^3}{x^3} = 1 - \frac{\tilde{x}_{\text{cfo}}^3}{x^3} + c_1 \frac{\tilde{x}_{\text{cfo}}^2}{x^3}. \quad (16)$$

The rapid approach to $m_{\chi,\text{eff}} = m_\chi$ after \tilde{x}_{cfo} drives χ out of equilibrium. This indicates the beginning of **coherent freeze-out**.

Using this expression in the Boltzmann equation and expanding $\sigma v = \sigma_0 + \sigma_1 v^2 + \dots$, the coherent freeze-out temperature x_{cfo} is found to be

$$x_{\text{cfo}} \approx \tilde{x}_{\text{cfo}} + \frac{1}{3} \log c + \frac{7}{6} \log \left(\frac{1}{3} \log c \right), \quad (17)$$

with

$$c \equiv \frac{27g_\chi}{2\pi^3} \sqrt{\frac{15}{2g_*}} m_\chi M_{\text{Pl}} (\sigma_0 + 6\sigma_1/\tilde{x}_{\text{cfo}}) \tilde{x}_{\text{cfo}}^{-4}. \quad (18)$$

The resulting asymptotic yield is

$$Y_{\chi,\infty}^{\text{cfo}} \approx \frac{14}{9} \sqrt{\frac{45}{\pi g_*}} \frac{1}{m_\chi M_{\text{Pl}}} \frac{x_{\text{cfo}}}{\sigma_0 + 21\sigma_1/(10x_{\text{cfo}})}. \quad (19)$$

The derivations of (17)-(19) are provided in Appendix C. These analytical expressions are highly accurate in the

small- κ regime, where $x_{\text{cfo}} \approx \tilde{x}_{\text{cfo}}$; deviations from the exact numerical results remain below 1% for $\tilde{x}_{\text{cfo}} \gtrsim 50$ (see Table I). The evolution of Y_χ with temperature is shown in Fig. 2.

At this point, it is interesting to compare the yield predicted in our mechanism with that in the standard freeze-out case:

$$\frac{Y_{\chi,\infty}^{\text{cfo}}}{Y_{\chi,\infty}^{\text{fo}}} = \frac{14}{9} \frac{x_{\text{cfo}}}{x_{\text{fo}}} \frac{\sigma_0^{\text{fo}} + 3\sigma_1^{\text{fo}}/x_{\text{fo}}}{\sigma_0^{\text{cfo}} + 21\sigma_1^{\text{cfo}}/(10x_{\text{cfo}})}, \quad (20)$$

where σ_i^{cfo} and σ_i^{fo} denote the annihilation cross sections in the coherent and standard freeze-out cases, respectively, and $x_{\text{fo}} \approx 25$ is the standard freeze-out temperature. For $\sigma_i^{\text{cfo}} = \sigma_i^{\text{fo}}$, we find an enhancement of the yield of order $x_{\text{cfo}}/x_{\text{fo}}$ for s -wave and $x_{\text{cfo}}^2/x_{\text{fo}}^2$ for p -wave annihilation. Since $x_{\text{cfo}} \sim \kappa^{-1/2} \gg 25$, the enhancement – especially for p -wave – is substantial.

If κ is extremely small, freeze-out may occur when χ is still relativistic. For instance, if WIMPs annihilate via exchanging weak gauge bosons, for temperatures below the weak scale, we have $\langle \sigma v \rangle_{\text{eff}} \sim m_{\chi,\text{eff}}^2 G_F^2/x^\ell \sim T^2 G_F^2/x^\ell$, with $\ell = 0$ ($\ell = 1$) for s -wave (p -wave), and G_F is the Fermi constant. Requiring $n_\chi \langle \sigma v \rangle_{\text{eff}} \sim H$ with $n_\chi \sim T^3$ gives the relativistic freeze-out temperatures:

$$T_{\text{rfo}}^s \sim G_F^{-2/3} M_{\text{Pl}}^{-1/3} \sim \text{MeV}, \quad (21)$$

$$T_{\text{rfo}}^p \sim G_F^{-1/2} \left(\frac{m_\chi}{M_{\text{Pl}}} \right)^{1/4} \sim 10 \text{ MeV} \left(\frac{m_\chi}{10 \text{ GeV}} \right)^{1/4}. \quad (22)$$

Relativistic freeze-out yields too large χ relic abundance, so viable models require $x_{\text{cfo}} < m_\chi/T_{\text{rfo}}$.

In the coherent freeze-out scenario, the WIMP annihilation cross section can exceed the standard value while still yielding the correct relic abundance. Fig. 3 shows the ratio of the required cross sections in the two scenarios, assuming both reproduce the observed DM density, where we fix $g_\chi = 4$. The $r = 1$ contour corresponds to $\kappa \approx 10^{-3}$. For $\kappa \gtrsim 10^{-3}$, the ALP symmetry is restored before $x_{\text{fo}} \approx 25$, reducing to the standard freeze-out case (gray region), whereas for $\kappa \lesssim 10^{-3}$ the coherent effect becomes significant.

Cosmic microwave background (CMB) anisotropies place stringent limits on the WIMP s -wave annihilation cross section σ_0 [16, 17]. For $m_\chi \lesssim 30$ GeV, the thermal value $\sigma_0^{\text{fo}} \approx 2.2 \times 10^{-26}$ cm³/s is excluded [18], with the bound weakening at higher masses. In the coherent freeze-out scenario, the required s -wave cross section can exceed the standard value, extending the CMB constraint to heavier WIMPs. This bound appears as the red dash-dotted line in Fig. 3, and the region below it is excluded for s -wave-dominated annihilation. Even under this constraint, the s -wave cross section can still be enhanced by up to two orders of magnitude before reaching the unitarity limit [19] (red dashed line).

In contrast, the enhancement needed for p -wave annihilation is much larger – scaling as $\propto x_{\text{cfo}}^2/x_{\text{fo}}^2$ rather than $\propto x_{\text{cfo}}/x_{\text{fo}}$ – and can reach values of order 10^5 in

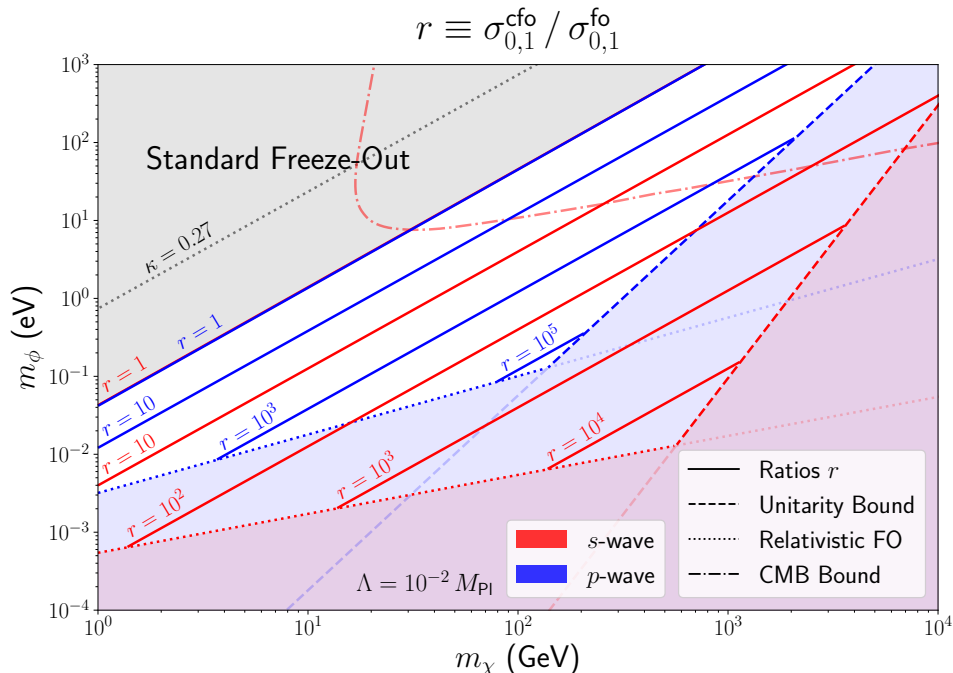


FIG. 3. Coherent freeze-out mechanism in the **FOPT** regime, where DM consists solely of the WIMP. For illustration, we fix the cutoff scale to $\Lambda = 10^{-2} M_{\text{Pl}}$. Contour lines show the ratio of WIMP annihilation cross sections in the coherent and standard freeze-out scenarios for s -wave (red solid) and p -wave (blue solid) processes, assuming both reproduce the observed relic abundance. Regions below the red (blue) dotted curves are excluded because freeze-out would occur while the WIMP is still relativistic for s -wave (p -wave). Regions to the right of the red (blue) dashed curves violate unitarity for s -wave (p -wave). The gray shaded region marks $r = 1$, where coherent and standard freeze-out coincide, and the black dotted line ($\kappa = 0.27$) separates the FOPT (below) and crossover (above) regimes. The red dash-dotted line shows the CMB constraint on the s -wave cross section, excluding the region below it. No analogous CMB bound applies to p -wave DM due to velocity suppression.

Fig. 3 before saturating unitarity. Consequently, p -wave-dominated WIMPs can have annihilation cross sections up to five orders of magnitude above the standard thermal value while still yielding the observed relic abundance. This greatly enlarges the viable parameter space and, strikingly, opens realistic prospects for the indirect detection of p -wave DM.

Finally, we comment on the ALP evolution after WIMP freeze-out. One might expect that ϕ also contributes to the relic abundance. During symmetry restoration, the field is first trapped in the symmetry-breaking vacuum and then undergoes non-adiabatic evolution. Subsequently, the field oscillates around $\phi = 0$, with the ALP energy density red-shifting as matter. An explicit estimate gives the ALP density after freeze-out: $\rho_\phi(T) \sim \kappa^{-1/2} m_\chi T^3$, which, if stable, would exceed the observed DM density and overclose the Universe. Thus, ϕ must be unstable, with a lifetime set by its model-dependent couplings to other species and not constrained in a universal way. We therefore conclude that in the FOPT regime, DM is composed solely of the WIMP.

B. Crossover regime

We now turn to the crossover regime, where the ALP evolution is nearly adiabatic. In this regime, the symmetry of the ALP potential is restored before $x_{\text{fo}} \approx 25$, so the ALP has little influence on the WIMP freeze-out. Instead, the thermal effect from the WIMP bath significantly alters the ALP evolution, producing a relic abundance that departs from the standard misalignment result. Consequently, the ALP can naturally serve as a second DM component in this regime.

Since the two sectors decouple while χ is still relativistic, we may take the limit $\gamma x \ll 1$ in the ALP EOM (8), which reduces to

$$\varphi'' + \frac{2}{x} \varphi' - \eta (1 - \kappa x^2) \varphi + \eta \varphi^3 = 0. \quad (23)$$

The symmetry is broken for $x < x_c \equiv 1/\sqrt{\kappa}$ and restored for $x > x_c$. As shown in Fig. 5, the ALP is initially frozen by Hubble friction for $x \ll 1/\sqrt{\eta}$; for $1/\sqrt{\eta} \lesssim x \lesssim x_c$, it evolves toward the symmetry-breaking minimum at $\varphi_* = 1$ and stabilizes there, erasing any dependence on its initial value; and for $x \gtrsim x_c$, the symmetry is restored and the field relaxes back toward $\varphi = 0$.

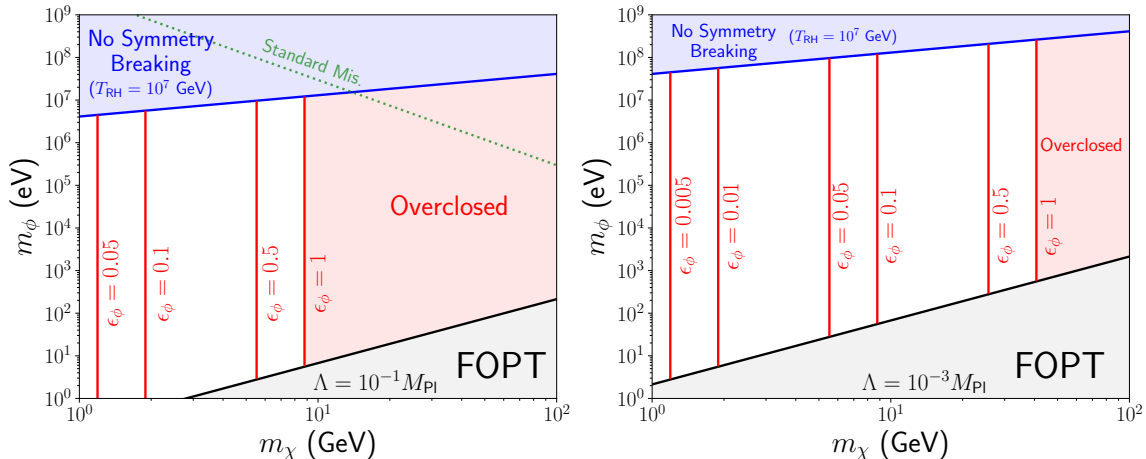


FIG. 4. Coherent freeze-out mechanism in the **crossover** regime, where DM may consist of both the WIMP and the ALP. We fix the cutoff scale to $\Lambda = 10^{-1}M_{\text{Pl}}$ (left) and $\Lambda = 10^{-3}M_{\text{Pl}}$ (right). Red contours show the ALP fraction $\epsilon_\phi \equiv \Omega_\phi/\Omega_{\text{DM}}$; regions with $\epsilon_\phi > 1$ overproduce ALP DM and are excluded. The area below the black line ($\kappa = 0.27$) corresponds to the FOPT regime, while regions above the blue line exhibit no symmetry breaking (relaxable with a higher reheating temperature). For comparison, the green dotted line shows the standard misalignment prediction of $\epsilon_\phi = 1$, using $\phi_i = \sqrt{m_\chi \Lambda}$ as the initial field displacement.

The adiabatic approximation holds when

$$\eta(1 - \kappa x^2) \gg 1/x^2, \quad (24)$$

i.e., when the effective ALP mass dominates over Hubble friction. This condition fails near x_c , where the thermal and bare mass terms cancel. We define $x_1 = x_c + \delta x$ by requiring $|\eta(1 - \kappa x_1^2)| \equiv 1/x_1^2$ so that adiabaticity is restored for $x > x_1$. In the limit $\eta \gg \kappa$ (which is always satisfied for the relevant parameter space), one finds $\delta x/x_c \approx \kappa/(2\eta)$, implying that the loss of adiabaticity is extremely brief.

For $x > x_1$, adiabatic evolution gives

$$m_{\phi,\text{eff}}(x)\phi^2(x)a^3(x) = m_{\phi,\text{eff}}(x_1)\phi^2(x_1)a^3(x_1), \quad (25)$$

where $a(x)$ is the cosmic scale factor. The quantity in (25) is the adiabatic invariant, corresponding to the conservation of the comoving ALP number density.

At present, $x_0 \equiv m_\chi/T_0$, the thermal mass is negligible, $m_{\chi,\text{eff}}(x_0) = m_\chi$, so we obtain

$$\frac{\phi^2(x_0)a^3(x_0)}{\phi^2(x_1)a^3(x_1)} = \frac{H(x_1)}{m_\phi} \approx \frac{H(x_c)}{m_\phi} = \left(\frac{\kappa}{\eta}\right)^{\frac{1}{2}} \ll 1. \quad (26)$$

This corresponds to a rapid drop in the ALP field around x_c during symmetry restoration, which agrees well with the numerical solution (see Fig. 6). The present-day energy density is therefore

$$\begin{aligned} \rho_\phi(x_0) &= m_\phi^2 \phi^2(x_1) \left(\frac{\kappa}{\eta}\right)^{\frac{1}{2}} \left(\frac{x_1}{x_0}\right)^3 \frac{g_{*S}(x_0)}{g_{*S}(x_1)} \\ &\approx m_\phi^2 \phi^2(x_c) \left(\frac{\kappa}{\eta}\right)^{\frac{1}{2}} \left(\frac{x_c}{x_0}\right)^3 \frac{g_{*S}(x_0)}{g_{*S}(x_c)}, \end{aligned} \quad (27)$$

where in the second line we used $x_1 \approx x_c$ for $\eta \gg \kappa$ and g_{*S} is the entropy-weighted number of relativistic degrees of freedom. Substituting $\phi(x_c) = \sqrt{m_\chi \Lambda}$ into (27) and using (7) and (9), we arrive at the relic abundance:

$$\begin{aligned} \Omega_\phi &= \frac{1.66 \cdot 4g_{*S}(x_0)\sqrt{2g_\chi g_*(x_c)}}{3g_{*S}(x_c)} \frac{m_\chi^{3/2} \Lambda^{1/2} T_0^3}{H_0^2 M_{\text{Pl}}^3} \\ &\approx 0.3 \left(\frac{m_\chi}{10 \text{ GeV}}\right)^{3/2} \left(\frac{\Lambda}{0.1 M_{\text{Pl}}}\right)^{1/2}, \end{aligned} \quad (28)$$

where to obtain the numerical value, we used $g_\chi = 4$, $g_{*S}(x_c) = g_*(x_c) = 106.75$, and $g_{*S}(x_0) = 3.93$.

We thus arrive at an “**ALP miracle**”: an ALP that couples quadratically to a weak-scale fermion with a Planck-suppressed interaction can naturally obtain the correct relic abundance. Importantly, this prediction is insensitive to both the initial ALP field value and the ALP mass, provided the latter lies in the crossover regime, $\text{eV} \lesssim m_\phi \lesssim \text{MeV}$ (see the right panel of Fig. 1).

In Fig. 4, we show contour lines of the ALP fraction $\epsilon_\phi \equiv \Omega_\phi/\Omega_{\text{DM}}$, where $\Omega_{\text{DM}} \simeq 0.26$ is the observed DM density [18]. For comparison, the dotted line shows the standard misalignment prediction of $\epsilon_\phi = 1$, obtained by taking the initial displacement $\phi_i = \sqrt{m_\chi \Lambda}$.

IV. CONCLUSIONS

In this Letter, we considered the cosmological dynamics of a WIMP-like fermion and an ALP-like scalar field. We found that even a tiny effective coupling between the WIMP and ALP fields can have a dramatic effect on

their evolution due to coherent forward scattering. At high temperatures, spontaneous symmetry breaking by the ALP field may be induced. The dynamics of the subsequent phase transition determine the present-day densities of both WIMPs and ALPs, which may deviate by many orders of magnitude from the predictions of the standard WIMP freeze-out and ALP misalignment production mechanisms. Many of the conventional experimental targets for WIMP and ALP searches need to be reconsidered in this scenario; for example, the indirect detection of a p -wave WIMP may become viable. This will be pursued in our future work [20]. In addition, part of the parameter space of our model predicts a strongly first-order phase transition associated with the WIMP freeze-out, potentially sourcing an observable gravitational-wave signal.

ACKNOWLEDGMENTS

We thank Kai Bartnick, Cédric Delaunay, and Seung J. Lee for useful discussions. This work is supported by the NSF grant PHY-2309456. SF is partially supported by the Boochever Fellowship at Cornell University.

Appendix A: Order of the Phase Transition

The potential in Eq. (6) is controlled by a single parameter κ . In this appendix, we determine how the order of the phase transition depends on κ .

Ginzburg-Landau theory provides a convenient framework for analyzing phase transitions in terms of an order parameter, which in our case is the ALP vacuum expectation value. Near the critical point, the effective Lagrangian can be expanded as

$$\mathcal{L} = \frac{1}{2}(\partial_\mu\phi)^2 - a(T)\phi^2 - b(T)\phi^4 - c(T)\phi^6 + \dots \quad (\text{A1})$$

The vacuum configuration $\langle\phi\rangle$ that minimizes the potential

$$V(\phi) = a(T)\phi^2 + b(T)\phi^4 + c(T)\phi^6 + \dots \quad (\text{A2})$$

is controlled primarily by the sign of the quadratic coefficient $a(T)$:

- $a > 0$: $\langle\phi\rangle = 0$ symmetric phase;
- $a < 0$: $\langle\phi\rangle \neq 0$ broken phase.

The temperature at which $a(T)$ changes sign defines the critical point, $a(T_c) = 0$. The order of the transition is determined by the quartic coefficient evaluated at T_c :

- $b(T_c) > 0$: crossover transition;
- $b(T_c) < 0$: first-order transition.

We can map the Ginzburg-Landau parameters onto the potential used in the main text, Eq. (6), by expanding it in powers of the normalized field φ . This yields

$$a(x) = \frac{1}{2}\left(\kappa - \frac{K_1(x)}{x}\right), \quad (\text{A3})$$

$$b(x) = \frac{1}{4}\left(\frac{3K_1(x)}{x} - K_2(x)\right). \quad (\text{A4})$$

This directly determines the temperature dependence of the quadratic and quartic terms relevant for diagnosing the order of the phase transition.

The critical value of κ , denoted κ_c , separates the first-order phase transition (FOPT) from the crossover regime. The boundary is obtained by setting the quartic coefficient to zero, $b(x) = 0$, which can be solved numerically and gives

$$x_{\text{tri}} \approx 1.33. \quad (\text{A5})$$

We identify this as the *tricritical temperature* – the value of x at which the nature of the transition changes. If the critical temperature $x_c \equiv m_\chi/T_c$ lies above (below) x_{tri} , the transition is first order (crossover).

At the tricritical point, both coefficients vanish,

$$a(x_{\text{tri}}) = 0, \quad b(x_{\text{tri}}) = 0, \quad (\text{A6})$$

marking the boundary between the two regimes. Substituting $x_{\text{tri}} = 1.33$ into $a(x) = 0$ yields

$$\kappa_c \approx 0.27. \quad (\text{A7})$$

The resulting classification of FOPT versus crossover in the (m_χ, m_ϕ) plane is shown by the red curves in the right panel of Fig. 1.

Whether symmetry breaking can occur in the early Universe is determined by the curvature of the ALP potential near the origin, given by the sign of Eq. (A3). Since $K_1(x)/x$ is a monotonically decreasing function of x , symmetry breaking is possible only if it already occurs at the reheating temperature T_{RH} . This requires

$$\kappa < \frac{K_1(x_{\text{RH}})}{x_{\text{RH}}}, \quad (\text{A8})$$

where $x_{\text{RH}} \equiv m_\chi/T_{\text{RH}}$. This condition is shown by the blue curves in the right panel of Fig. 1; above these lines, no phase transition occurs at any time during cosmic evolution.

Appendix B: Full Solutions of the ALP Equation of Motion

The numerical solutions to the ALP equation of motion (8) are shown in Fig. 5 for both the FOPT and crossover regimes. Throughout, we assume that the ALP field has negligible initial velocity after inflation. To demonstrate the robustness of the evolution, we display trajectories

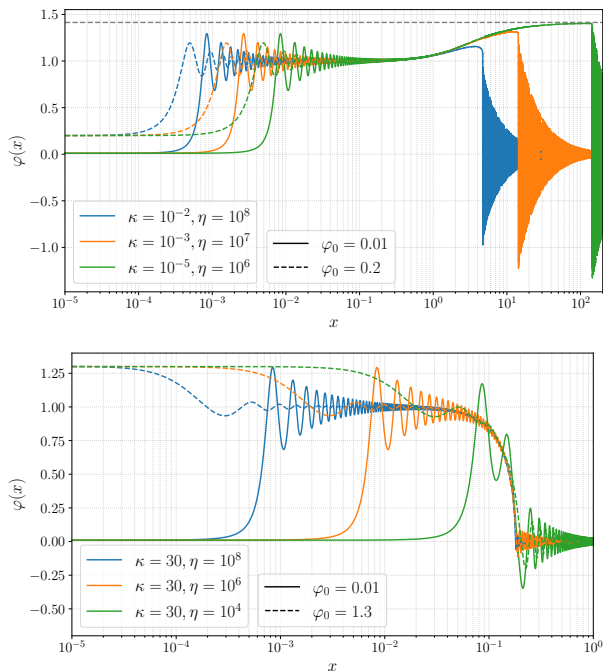


FIG. 5. Evolution of the ALP field in the first-order phase transition regime (upper panel) and the crossover regime (lower panel). Different colors correspond to different choices of κ and η , while different line styles denote different initial field displacements.

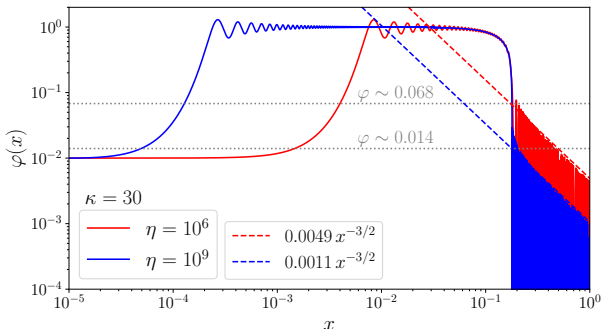


FIG. 6. Zoomed-in view of the ALP evolution for $\eta = 10^6$ (red) and $\eta = 10^9$ (blue) in the crossover regime with fixed $\kappa = 30$. Dashed lines indicate the matter-like scaling behavior, with normalization chosen to match the corresponding ALP trajectories.

with different initial displacements, $\varphi_0 = 10^{-2}$, 0.2, and 1.3 (different line styles). As the figure illustrates, the qualitative dynamics of the ALP field are insensitive to its initial value.

In the upper panel of Fig. 5, which shows the solution for $\varphi(x)$ in the FOPT regime ($\kappa < 0.27$), two distinct stages of oscillation are visible. First, the field oscillates about the symmetry-breaking minimum, located near $\varphi = 1$ and drifting toward $\sqrt{2}$ as x increases. This be-

havior matches the black curves in Fig. 1 and also Fig. 7, where the displaced minimum approaches $\sqrt{2}$ before disappearing at \tilde{x}_{cfo} . The onset of these early oscillations is controlled by η : larger η (blue curve) leads to an earlier departure from Hubble friction. At $x = \tilde{x}_{\text{cfo}} \sim \kappa^{-1/2}$, the symmetry-breaking minimum vanishes, and the field rolls toward the origin, initiating a second set of oscillations that resemble standard misalignment. The onset of this phase is governed by κ , with smaller κ (green curve) corresponding to a larger value of \tilde{x}_{cfo} .

In the lower panel of Fig. 5 we show the crossover regime ($\kappa > 0.27$), where the minimum of the potential smoothly evolves from $\varphi = 1$ to $\varphi = 0$. As in the FOPT case, the onset of the initial oscillations is controlled by η : larger η causes the field to leave the Hubble-frozen regime earlier. Unlike the FOPT regime, however, the vacuum does not drift toward $\varphi = \sqrt{2}$; instead, it continuously interpolates from $\varphi = 1$ to $\varphi = 0$. The parameter κ again determines when symmetry restoration occurs and thus when the second set of oscillations begins.

A key feature of the crossover regime is the rapid drop of the field value during symmetry restoration, a direct consequence of the nearly adiabatic evolution predicted by Eq. (26). This behavior underlies the ‘‘ALP miracle’’ and is numerically confirmed in Fig. 6. For $\kappa = 30$ and $\eta = 10^6$ (10^9), Eq. (26) predicts a drop of order $(\kappa/\eta)^{1/4} \approx 0.074$ (0.013) near $x_c = 1/\sqrt{\kappa} \approx 0.18$. Just before the drop, Fig. 6 shows $\varphi \approx 1$; the gray dotted lines at $\varphi \approx 0.068$ and 0.014 mark the post-drop values for $\eta = 10^6$ and 10^9 , respectively, prior to the onset of matter-like redshifting. The agreement with the analytical prediction is especially good for $\eta = 10^9$, as the adiabatic approximation becomes increasingly accurate at larger η , consistent with Eq. (24). This validates the analytical treatment used in the main text for the range of η relevant to the ALP-miracle window in Fig. 4, namely $\eta \sim 10^{16} - 10^{19}$.

Appendix C: WIMP Dynamics in the Strong First-Order Phase Transition Region

1. Evolution of the ALP Vacuum

When the symmetry is broken, the displaced vacuum $\varphi_* \neq 0$ is determined by the nonzero solution of

$$\begin{aligned} \frac{\partial \mathcal{V}(\varphi, x)}{\partial \varphi} &= \kappa \varphi - \frac{\varphi^3}{2} (1 - \varphi^2/2)^2 K_0(x(1 - \varphi^2/2)) \\ &\quad - \frac{\varphi}{2x} (2 - 3\varphi^2 + \varphi^4) K_1(x(1 - \varphi^2/2)) = 0, \end{aligned} \quad (\text{C1})$$

where \mathcal{V} is given by (6). This equation can be solved numerically for any fixed κ , as shown in Fig. 7. We are particularly interested in the small- κ limit relevant for a strong FOPT. Neglecting the κ term, the condition

simplifies to

$$\frac{\gamma_* x K_0(\gamma_* x)}{K_1(\gamma_* x)} = \frac{2(\varphi_*^2 - 1)}{\varphi_*^2}, \quad (\text{C2})$$

where $\gamma_* \equiv 1 - \varphi_*^2/2$ is the boost factor evaluated at the symmetry-breaking vacuum. The solution of $\varphi_*(x)$ is shown in Fig. 7: one finds $\varphi_*(x) \rightarrow 1$ for $x \ll 1$ and $\varphi_*(x) \rightarrow \sqrt{2}$ for $x \gg 1$ (consistent with Fig. 5).

An interesting feature emerges in the large- x limit: the product of the boost factor and inverse temperature approaches a constant (see the lower panel of Fig. 7):

$$\gamma_* x \approx 1.33. \quad (\text{C3})$$

(This numerical value corresponds to the root of the transcendental equation $cK_0(c) = K_1(c)$ where $c \equiv \gamma_* x$.)

This result has a striking impact on WIMP freeze-out. If κ is sufficiently small, the evolution of the symmetry-breaking vacuum described by Eq. (C2) remains a good approximation even at $x \gg 1$. In this regime, the effective WIMP mass satisfies $m_{\chi, \text{eff}}/T = \gamma_* x \approx 1.33$, implying that the WIMP remains in thermal equilibrium regardless of how large the bare ratio $x \equiv m_\chi/T$ becomes. Freeze-out can therefore occur only after symmetry is restored (corresponding to the jump in Fig. 7), when the ALP rolls back to the origin and $m_{\chi, \text{eff}} \rightarrow m_\chi$. As a result, the coherent freeze-out temperature T_{cfo} can be far lower than in the standard scenario, allowing $x_{\text{cfo}} \equiv m_\chi/T_{\text{cfo}} \gg \mathcal{O}(25)$. This delay enhances the WIMP relic abundance relative to the standard case. In the next subsection, we quantify this effect.

2. WIMP Relic Abundance

The Boltzmann equation that governs χ freeze-out dynamics is given by

$$\frac{dn_\chi}{dt} + 3Hn_\chi = -\langle\sigma v\rangle_{\text{eff}}(n_\chi^2 - n_{\chi, \text{eq}}^2), \quad (\text{C4})$$

where n_χ is the number density of χ and $\langle\sigma v\rangle_{\text{eff}}$ is the effective cross section of two χ particles annihilating to SM particles. In the medium of the ALP background, the effective mass of the WIMP is shifted from m_χ to $m_{\chi, \text{eff}} = \gamma(\varphi)m_\chi$, where $\gamma(\varphi) = |1 - \varphi^2/2|$ is the field-dependent boost factor. As a result, the effective annihilation cross section is also modified.

We assume that χ couples to SM species through a weak-scale interaction; therefore, we have $\langle\sigma v\rangle_{\text{eff}} \sim 1/(m_{\chi, \text{eff}}^2 x^\ell)$ for $m_{\chi, \text{eff}} \gtrsim m_M$ and $\langle\sigma v\rangle_{\text{eff}} \sim m_{\chi, \text{eff}}^2/(m_M^4 x^\ell)$ for $m_{\chi, \text{eff}} \lesssim m_M$, where m_M denotes the mass of the mediator that mediates the interaction between WIMP and SM particles, typically of the weak scale, and $\ell = 0$ ($\ell = 1$) for s -wave (p -wave). Putting them together, we can write $\langle\sigma v\rangle_{\text{eff}} \sim \min\{1/(\gamma^2 m_\chi^2 x^\ell), \gamma^2 m_\chi^2/(m_M^4 x^\ell)\}$.

We are interested in the effect of the ALP field on WIMP freeze-out dynamics. In the crossover region, the

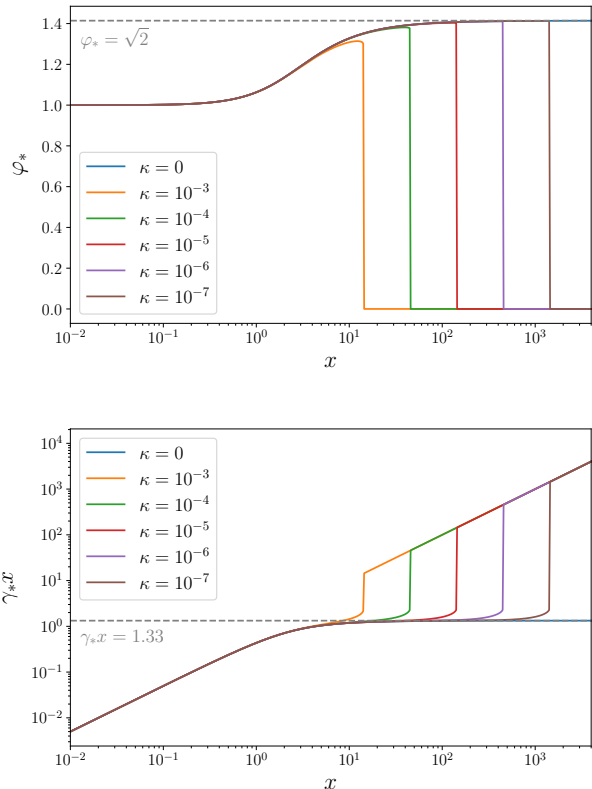


FIG. 7. The evolution of the symmetry-breaking vacuum φ_* (above) and the boost factor $\gamma_* \equiv 1 - \varphi_*^2/2$ (below) as a function of the inverse temperature $x \equiv m_\chi/T$.

symmetry of the ALP potential is restored earlier, typically at $x < x_{\text{fo}} \approx 25$, so the effect on freeze-out is negligible. By contrast, the effect is significant in the strong FOPT region with $\kappa \ll 1$, as we discuss below.

From Fig. 7, it can be seen that the boost factor scales as $\gamma \sim 1/x$ for $x \gg 1$, which suppresses $m_{\chi, \text{eff}}$ to keep it well below m_M . Therefore, we can factor out the dependence of the annihilation cross section on the ALP field value:

$$\langle\sigma v\rangle_{\text{eff}} = \gamma^2 \langle\sigma v\rangle, \quad (\text{C5})$$

where $\langle\sigma v\rangle \sim m_\chi^2/(m_M^4 x^\ell)$ is the *bare* annihilation cross section that does not depend on φ . In the non-relativistic limit, we can expand the bare cross section over the velocity: $\sigma v = \sigma_0 + \sigma_1 v^2 + \dots$, where σ_0 (σ_1) denotes the s -wave (p -wave) cross section. After the thermal average, it becomes $\langle\sigma v\rangle = \sigma_0 + 6\sigma_1/x + \dots$. We neglect terms more suppressed than p -wave. The equilibrium number density of χ is also affected by φ through the effective mass of χ (assuming a Maxwell-Boltzmann distribution of the χ bath):

$$n_{\chi, \text{eq}} = \frac{g_\chi}{2\pi^2} m_{\chi, \text{eff}}^2 T K_2(m_{\chi, \text{eff}}/T). \quad (\text{C6})$$

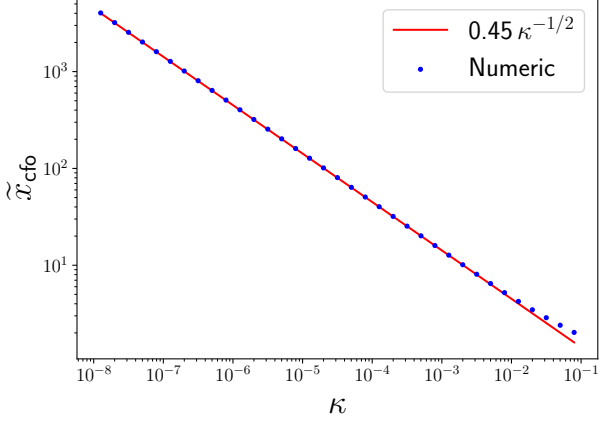


FIG. 8. \tilde{x}_{cfo} as a function of κ . The blue dots show the numerical solution of Eq. (C10), and the red line denotes the fitting function $\tilde{x}_{\text{cfo}} = 0.45 \kappa^{-1/2}$. The agreement is excellent in the small- κ regime.

Introducing the yield $Y_\chi \equiv n_\chi/s$ with s the entropy density, the Boltzmann equation (C4) is reduced to

$$Y'_\chi(x) = -\frac{\lambda\gamma^2}{x^2} \left(1 + \frac{b}{x}\right) [Y_\chi^2(x) - Y_{\chi,\text{eq}}^2(x)], \quad (\text{C7})$$

where $b \equiv 6\sigma_1/\sigma_0$, and

$$\lambda \equiv \sqrt{\frac{\pi}{45}} \frac{g_{*S}}{\sqrt{g_*}} m_\chi M_{\text{Pl}} \sigma_0, \quad (\text{C8})$$

$$Y_{\chi,\text{eq}}(x) \equiv \frac{n_{\chi,\text{eq}}}{s} = \frac{45g_\chi}{4\pi^4 g_{*S}} \gamma^2 x^2 K_2(\gamma x), \quad (\text{C9})$$

with g_* and g_{*S} denoting the number of relativistic degrees of freedom relevant to energy and entropy, respectively. Note that the equilibrium yield, $Y_{\chi,\text{eq}}$, depends essentially on $\gamma x = m_{\chi,\text{eff}}/T$ rather than m_χ/T .

In the broken phase, the ALP field is located at the symmetry-breaking vacuum $\varphi_* \neq 0$, reducing the effective WIMP mass. In the small- κ limit, $\gamma x = m_{\chi,\text{eff}}/T \approx 1.33$ remains a constant (see Fig. 7 and Eq. (C3)) regardless of how large the value of $x = m_\chi/T$ is. This allows WIMP to stay in equilibrium even at $x \gg \mathcal{O}(25)$. The local minimum at φ_* disappears at \tilde{x}_{cfo} , defined by

$$\left. \frac{\partial^2 \mathcal{V}(\varphi, \tilde{x}_{\text{cfo}})}{\partial \varphi^2} \right|_{\varphi=\varphi_*} = 0. \quad (\text{C10})$$

The solution of (C10) is shown in Fig. 8. For $\kappa \ll 1$, it can be fitted by a simple power law

$$\tilde{x}_{\text{cfo}} \approx 0.45 \kappa^{-1/2}. \quad (\text{C11})$$

At $x > \tilde{x}_{\text{cfo}}$, the ALP rolls back to the origin with a matter-like equation of state (one can check that $m_\phi >$

H is always satisfied at \tilde{x}_{cfo} for the parameter space of interest). Averaging over a period, it gives

$$\varphi(x > \tilde{x}_{\text{cfo}}) = (\tilde{x}_{\text{cfo}}/x)^{3/2} \varphi_*. \quad (\text{C12})$$

Therefore, the boost factor at $x > \tilde{x}_{\text{cfo}}$ scales as

$$\gamma = 1 - \frac{\varphi_*^2(\tilde{x}_{\text{cfo}})}{2} \frac{\tilde{x}_{\text{cfo}}^3}{x^3} \approx 1 - \frac{\tilde{x}_{\text{cfo}}^3}{x^3}, \quad (\text{C13})$$

where the approximation holds if $\tilde{x}_{\text{cfo}} \gg 1$. We see from (C13) that after \tilde{x}_{cfo} , the effective mass of the WIMP tends to its bare mass rapidly as $\gamma \rightarrow 1$, which triggers the freeze-out. Substituting (C13) into the Boltzmann equation (C7) determines the freeze-out temperature x_{cfo} . The numerical solution of (C7) is shown in Fig. 2. In the following, we show how to calculate x_{cfo} and the final yield analytically.

Our approximate analytical method is inspired by the method in [21] that applies to the standard freeze-out case. Before freeze-out ($x < x_{\text{cfo}}$), the yield can track closely with the equilibrium value, $Y_\chi \approx Y_{\chi,\text{eq}}$, so (C7) becomes

$$Y_\chi - Y_{\chi,\text{eq}} \approx -\frac{x^2}{2\lambda\gamma^2(1+b/x)} \frac{Y'_{\chi,\text{eq}}}{Y_{\chi,\text{eq}}}. \quad (\text{C14})$$

Using the non-relativistic expansion that satisfies at $\gamma x \gg 1$, we have $Y_{\chi,\text{eq}} \approx a(\gamma x)^{3/2} e^{-\gamma x}$, where $a \equiv 45g_\chi/(4\sqrt{2}\pi^{7/2}g_{*S})$ is roughly a constant during freeze-out. Using (C13), we obtain

$$\frac{Y'_{\chi,\text{eq}}}{Y_{\chi,\text{eq}}} \approx -\left(1 + 2\frac{\tilde{x}_{\text{cfo}}^3}{x^3}\right), \quad \text{for } x > \tilde{x}_{\text{cfo}} \gg 1. \quad (\text{C15})$$

We define the freeze-out temperature x_{cfo} as the time after which Y_χ fails to track $Y_{\chi,\text{eq}}$,

$$Y_\chi(x_{\text{cfo}}) - Y_{\chi,\text{eq}}(x_{\text{cfo}}) \equiv Y_{\chi,\text{eq}}(x_{\text{cfo}}). \quad (\text{C16})$$

Combining Eqs. (C13)-(C16), we obtain

$$\begin{aligned} x_{\text{cfo}}^{1/2} \left(1 + 2\frac{\tilde{x}_{\text{cfo}}^3}{x_{\text{cfo}}^3}\right) e^{(1-\tilde{x}_{\text{cfo}}^3/x_{\text{cfo}}^3)x_{\text{cfo}}} \\ = 2a\lambda \left(1 + \frac{b}{x_{\text{cfo}}}\right) \left(1 - \frac{\tilde{x}_{\text{cfo}}^3}{x_{\text{cfo}}^3}\right)^{7/2}. \end{aligned} \quad (\text{C17})$$

Because freeze-out occurs rapidly after \tilde{x}_{cfo} , we have $\Delta x \equiv x_{\text{cfo}} - \tilde{x}_{\text{cfo}} \ll \tilde{x}_{\text{cfo}}$. Note that the non-relativistic approximation of $Y_{\chi,\text{eq}}$ used above requires $3\Delta x \gg 1$. Up to the leading order of $\Delta x/\tilde{x}_{\text{cfo}}$, the above equation is reduced to

$$(\Delta x)^{-7/2} e^{3\Delta x} = 18\sqrt{3} a\lambda (1 + b/\tilde{x}_{\text{cfo}}) \tilde{x}_{\text{cfo}}^{-4}. \quad (\text{C18})$$

This can be solved iteratively, which leads to the freeze-out temperature

$$\begin{aligned} x_{\text{cfo}} \approx \tilde{x}_{\text{cfo}} + \frac{1}{3} \log \left(18\sqrt{3} a\lambda (1 + b/\tilde{x}_{\text{cfo}}) \tilde{x}_{\text{cfo}}^{-4} \right) \\ + \frac{7}{6} \log \left[\frac{1}{3} \log \left(18\sqrt{3} a\lambda (1 + b/\tilde{x}_{\text{cfo}}) \tilde{x}_{\text{cfo}}^{-4} \right) \right]. \end{aligned} \quad (\text{C19})$$

		Analytic	Numeric	Error
$\kappa = 10^{-3}$	x_{cfo}	23	29	21%
	$Y_\infty (\times 10^{-13})$	4.1	5.4	24%
$\kappa = 10^{-4}$	x_{cfo}	52	53	1.9%
	$Y_\infty (\times 10^{-12})$	1.31	1.30	0.77%
$\kappa = 10^{-5}$	x_{cfo}	147.9	148.0	0.07%
	$Y_\infty (\times 10^{-12})$	4.15	4.13	0.48%
$\kappa = 10^{-6}$	x_{cfo}	455.3	455.4	0.02%
	$Y_\infty (\times 10^{-11})$	1.31	1.32	0.76%

TABLE I. Comparison between the approximate analytical formulae (C19) and (C22) with the numerical results. The benchmark parameters used are $m_\chi = 1$ TeV and $\sigma_0 = 2.2 \times 10^{-26} \text{ cm}^3/\text{s}$ (for s -wave annihilation).

The analytical formula in (C19) is accurate in the limit of $\kappa \ll 1$ (corresponding to $\tilde{x}_{\text{cfo}} \gg 1$). Note that the value of Δx decreases as κ decreases. For sufficiently small κ , the condition $3\Delta x \gg 1$ breaks down, so that the above non-relativistic expansion of $Y_{\chi,\text{eq}}$ fails. In this case, it is a good approximation to take $x_{\text{cfo}} \approx \tilde{x}_{\text{cfo}}$.

Next, we move on to calculate the yield. After freeze-out, $Y_{\chi,\text{eq}}$ is negligible compared to Y_χ , so the Boltzmann equation (C7) is reduced to

$$\frac{dY_\chi}{Y_\chi^2} = -\frac{\lambda}{x^2} \left(1 + \frac{b}{x}\right) \left(1 - \frac{\tilde{x}_{\text{cfo}}^3}{x^3}\right)^2 dx. \quad (\text{C20})$$

Integrating from x_{cfo} to infinity at both sides leads to

$$\frac{1}{Y_{\chi,\infty}} - \frac{1}{Y_\chi(x_{\text{cfo}})} = \frac{\lambda}{x_{\text{cfo}}} \left(1 - \frac{1}{2} \frac{\tilde{x}_{\text{cfo}}^3}{x_{\text{cfo}}^3} + \frac{1}{7} \frac{\tilde{x}_{\text{cfo}}^6}{x_{\text{cfo}}^6}\right) + \frac{b\lambda}{2x_{\text{cfo}}^2} \left(1 - \frac{4}{5} \frac{\tilde{x}_{\text{cfo}}^3}{x_{\text{cfo}}^3} + \frac{1}{4} \frac{\tilde{x}_{\text{cfo}}^6}{x_{\text{cfo}}^6}\right) \quad (\text{C21})$$

where the first (second) line denotes the contribution from s -wave (p -wave). Up to the leading order of $\Delta x/\tilde{x}_{\text{cfo}}$, the final yield in the coherent freeze-out scenario is given by

$$\begin{aligned} Y_{\chi,\infty}^{\text{cfo}} &\approx \frac{14}{9} \frac{x_{\text{cfo}}}{\lambda} \frac{1}{1 + 7b/(20x_{\text{cfo}})} \\ &= \frac{14}{9} \sqrt{\frac{45g_*}{\pi g_{*S}}} \frac{1}{m_\chi M_{\text{Pl}} \sigma_0 + 21\sigma_1/(10x_{\text{cfo}})}, \end{aligned} \quad (\text{C22})$$

where in the second line we have used the relation $b = 6\sigma_1/\sigma_0$ and (C8).

In Table I, we compare the analytical expressions for the freeze-out temperature (C19) and final yield (C22) with the results obtained from a full numerical solution of the Boltzmann equation (C7). As expected, the analytical formulae become increasingly accurate in the small- κ (large- x_{cfo}) regime. Indeed, Table I shows that they already achieve $\sim 1\%$ accuracy for $x_{\text{cfo}} \gtrsim 50$, corresponding to $\kappa \lesssim 10^{-4}$.

As a reference point, the standard freeze-out mechanism predicts a final yield [1]

$$Y_{\chi,\infty}^{\text{fo}} = \sqrt{\frac{45g_*}{\pi g_{*S}}} \frac{1}{m_\chi M_{\text{Pl}}} \frac{x_{\text{fo}}}{\sigma_0 + 3\sigma_1/x_{\text{fo}}}, \quad (\text{C23})$$

with $x_{\text{fo}} \approx 25$. Assuming the same annihilation cross section, the coherent freeze-out mechanism predicts a final yield larger than the standard freeze-out by

$$\frac{Y_{\chi,\infty}^{\text{cfo}}}{Y_{\chi,\infty}^{\text{fo}}} = \frac{14}{9} \frac{x_{\text{cfo}}}{x_{\text{fo}}} \frac{\sigma_0 + 3\sigma_1/x_{\text{fo}}}{\sigma_0 + 21\sigma_1/(10x_{\text{cfo}})}. \quad (\text{C24})$$

For s -wave-dominated annihilation, the relic abundance is therefore enhanced by a factor of $x_{\text{cfo}}/x_{\text{fo}}$. If χ is a Majorana fermion, the s -wave annihilation to a light SM fermion-antifermion pair ($\chi\chi \rightarrow f\bar{f}$) is helicity suppressed by m_f^2/m_χ^2 [22], and for $m_\chi < m_W$ the annihilation is typically p -wave dominated. Taking $\sigma_0 \ll \sigma_1$ in (C24), we obtain the enhancement factor for p -wave:

$$\left. \frac{Y_{\chi,\infty}^{\text{cfo}}}{Y_{\chi,\infty}^{\text{fo}}} \right|_{p\text{-wave}} = \frac{20}{9} \frac{x_{\text{cfo}}^2}{x_{\text{fo}}^2}, \quad (\text{C25})$$

which is much more significant than the s -wave case. This result is remarkable: it allows σ_1 to exceed the standard thermal value by a factor of $(x_{\text{cfo}}/x_{\text{fo}})^2$ while still producing the correct relic abundance, thereby opening the possibility of the indirect detection of p -wave DM.

Appendix D: Full One-loop Thermal Potential

In the main text, we introduced two simplifying assumptions to gain analytical insight into the coherent freeze-out mechanism: (i) we neglected quantum-statistical effects by using the classical Maxwell-Boltzmann (MB) distribution instead of the Fermi-Dirac (FD) distribution for the WIMP thermal bath, and (ii) we ignored higher-order corrections in φ , retaining only the quadratic term in the one-loop thermal potential. (After including the back-reaction, the resulting potential also contains a term quartic in φ , ensuring it remains bounded from below.) In this appendix, we show that incorporating both effects does not alter the qualitative picture presented in the main text.

First, we compare the ALP thermal-mass contribution $m_\phi^2 \rightarrow m_\phi^2 - \langle \bar{\chi}\chi \rangle_T/\Lambda$ obtained using the MB and FD distributions. Substituting $f_\chi^{\text{MB}} = e^{-E_\chi/T}$ and $f_\chi^{\text{FD}} = 1/(e^{E_\chi/T} + 1)$ into (4) gives

$$\begin{aligned} \langle \bar{\chi}\chi \rangle_T^{\text{MB}} &= \frac{g_\chi m_{\chi,\text{eff}}}{2\pi^2} \int_{m_{\chi,\text{eff}}}^{\infty} dE (E^2 - m_{\chi,\text{eff}}^2)^{1/2} e^{-E/T} \\ &= \frac{g_\chi}{2\pi^2} m_{\chi,\text{eff}}^2 TK_1(m_{\chi,\text{eff}}/T), \end{aligned} \quad (\text{D1})$$

$$\langle \bar{\chi}\chi \rangle_T^{\text{FD}} = \frac{g_\chi m_{\chi,\text{eff}}}{2\pi^2} \int_{m_{\chi,\text{eff}}}^{\infty} dE (E^2 - m_{\chi,\text{eff}}^2)^{1/2} \frac{1}{e^{E/T} + 1}. \quad (\text{D2})$$

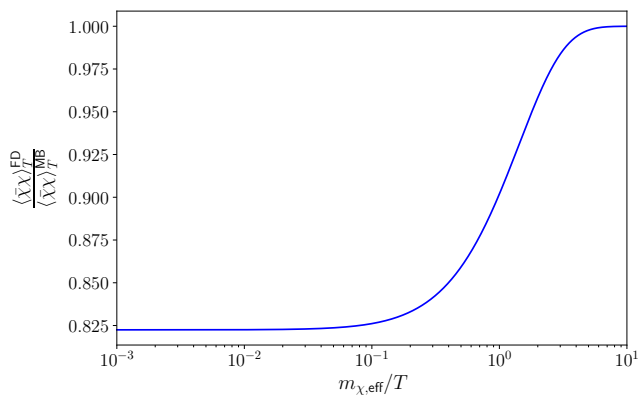


FIG. 9. Ratio of the Fermi-Dirac to Maxwell-Boltzmann contributions to the ALP thermal mass as a function of $m_{\chi,\text{eff}}/T$. The ratio approaches 0.82 in the relativistic limit and 1 in the nonrelativistic limit.

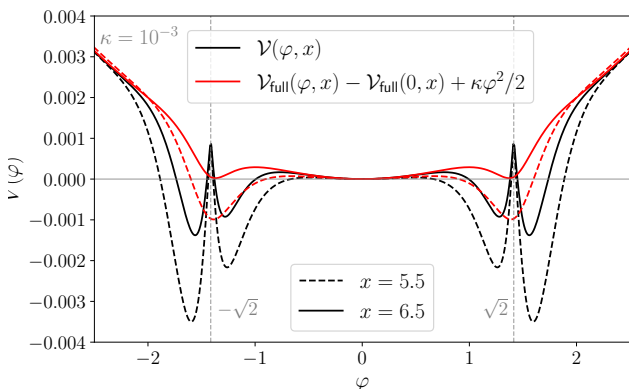


FIG. 10. Comparison between the full one-loop thermal potential $\mathcal{V}_{\text{full}}$ (red) and the approximate potential \mathcal{V} used in the main text (6) (black) in the FOPT regime ($\kappa = 10^{-3}$), shown for several values of x . For clarity, the field-independent part of $\mathcal{V}_{\text{full}}$ has been subtracted and the bare scalar mass term is included. The cusp at $\varphi = \pm\sqrt{2}$ (vertical dashed line) marks $m_{\chi,\text{eff}} = 0$, beyond which the approximate potential breaks down and higher-order terms in φ become important.

The FD expression does not admit a simple closed form.

In the relativistic limit, $T \gg m_{\chi,\text{eff}}$, both reduce to

$$\langle \bar{\chi}\chi \rangle_T^{\text{MB}} \approx \frac{g_\chi}{2\pi^2} m_{\chi,\text{eff}} T^2 \quad (\text{D3})$$

$$\langle \bar{\chi}\chi \rangle_T^{\text{FD}} \approx \frac{g_\chi}{24} m_{\chi,\text{eff}} T^2. \quad (\text{D4})$$

Thus, the two results differ by a factor of $\pi^2/(12) \approx 0.82$ in the relativistic limit and converge in the nonrelativistic limit (see Fig. 9). Using the MB distribution instead of the FD distribution therefore induces an error of less than 20%.

Next, we consider corrections from higher-order terms in φ . The potential used in the main text is only valid for $\varphi \lesssim \mathcal{O}(1)$; for $\varphi \gg \mathcal{O}(1)$, one must include contributions from higher powers in φ . Given the coupling in (1), the full one-loop thermal potential of ϕ in a χ thermal bath can be computed using standard thermal field theory (see, e.g., [23]). The result is given by (ignoring the bare mass term):

$$\begin{aligned} \mathcal{V}_{\text{full}}(\phi, T) &= -\frac{g_\chi}{2\pi^2} T^4 \int_0^\infty dy y^2 \log \left[1 + e^{-\sqrt{y^2 + m_{\chi,\text{eff}}^2}/T} \right] \\ &\equiv \frac{g_\chi}{2\pi^2} m_\chi^4 \mathcal{V}_{\text{full}}(\varphi, x), \end{aligned} \quad (\text{D5})$$

with the dimensionless potential defined as

$$\mathcal{V}_{\text{full}}(\varphi, x) = \frac{-1}{x^4} \int_0^\infty dy y^2 \log \left[1 + e^{-\sqrt{y^2 + \gamma^2 x^2}} \right], \quad (\text{D6})$$

where $\gamma(\varphi) \equiv |1 - \varphi^2/2|$. Expanding (D5) in the relativistic limit $\gamma x \ll 1$ and keeping terms up to $\mathcal{O}(\varphi^2)$, one recovers exactly (D4), the thermal correction to the quadratic term. This confirms that the quadratic approximation is valid for our analysis in the crossover regime, where the decoupling occurs well before WIMP freeze-out and the condition $\gamma x \ll 1$ is always satisfied.

In the FOPT regime, decoupling occurs much later, but the ALP remains trapped in the symmetry-breaking vacuum, yielding $\gamma x \approx 1.33$. Consequently, the relativistic expansion still remains a good approximation. Fig. 10 compares the full thermal potential (D6) with the approximate form (6) used in the main text. The full potential likewise develops a symmetry-breaking minimum near $\varphi = \pm\sqrt{2}$ and, crucially, shows the characteristic degenerate vacua associated with a first-order transition at small κ . This confirms that the qualitative dynamics described in the main text, including the delayed symmetry restoration and the trapping of the ALP field, persist beyond the quadratic approximation. In particular, WIMP freeze-out can still be significantly delayed for sufficiently small κ . A full numerical analysis of coherent freeze-out in the FOPT regime using the complete thermal potential (D6) is required for precision relic-density predictions, but we leave this to future work.

-
- [1] M. Cirelli, A. Strumia, and J. Zupan, (2024), [arXiv:2406.01705 \[hep-ph\]](#).
 - [2] D. J. E. Marsh, *Phys. Rept.* **643**, 1 (2016), [arXiv:1510.07633 \[astro-ph.CO\]](#).
 - [3] F. Piazza and M. Pospelov, *Phys. Rev. D* **82**, 043533 (2010), [arXiv:1003.2313 \[hep-ph\]](#).
 - [4] T. Moroi, K. Mukaida, K. Nakayama, and M. Takimoto, *JHEP* **06**, 040 (2013), [arXiv:1304.6597 \[hep-ph\]](#).
 - [5] B. Lillard, M. Ratz, T. Tait, M. P., and S. Trojanowski, *JCAP* **07**, 056 (2018), [arXiv:1804.03662 \[hep-ph\]](#).
 - [6] S. Ramazanov, E. Babichev, D. Gorbunov, and A. Vikman, *Phys. Rev. D* **105**, 063530 (2022), [arXiv:2104.13722 \[hep-ph\]](#).
 - [7] B. Batell and A. Ghalsasi, *Phys. Rev. D* **107**, L091701 (2023), [arXiv:2109.04476 \[hep-ph\]](#).
 - [8] A. Banerjee, N. H. Nguyen, and E. H. Tanin, (2025), [arXiv:2509.25308 \[hep-ph\]](#).
 - [9] P. W. Graham, H. Ramani, O. Simon, and E. H. Tanin, (2025), [arXiv:2511.09614 \[hep-ph\]](#).
 - [10] E. Epelbaum, H.-W. Hammer, and U.-G. Meissner, *Rev. Mod. Phys.* **81**, 1773 (2009), [arXiv:0811.1338 \[nucl-th\]](#).
 - [11] R. Machleidt and D. R. Entem, *Phys. Rept.* **503**, 1 (2011), [arXiv:1105.2919 \[nucl-th\]](#).
 - [12] A. Hook and J. Huang, *JHEP* **06**, 036 (2018), [arXiv:1708.08464 \[hep-ph\]](#).
 - [13] F. Bigazzi, A. L. Cotrone, M. Järvinen, and E. Kiritsis, *JHEP* **01**, 100 (2020), [arXiv:1906.12132 \[hep-ph\]](#).
 - [14] L. Di Luzio, M. Giannotti, E. Nardi, and L. Visinelli, *Phys. Rept.* **870**, 1 (2020), [arXiv:2003.01100 \[hep-ph\]](#).
 - [15] H. Fukuda and S. Shirai, *Phys. Rev. D* **105**, 095030 (2022), [arXiv:2112.13536 \[hep-ph\]](#).
 - [16] T. R. Slatyer, *Phys. Rev. D* **93**, 023527 (2016), [arXiv:1506.03811 \[hep-ph\]](#).
 - [17] T. R. Slatyer, *Phys. Rev. D* **93**, 023521 (2016), [arXiv:1506.03812 \[astro-ph.CO\]](#).
 - [18] N. Aghanim *et al.* (Planck), *Astron. Astrophys.* **641**, A6 (2020), [Erratum: *Astron. Astrophys.* 652, C4 (2021)], [arXiv:1807.06209 \[astro-ph.CO\]](#).
 - [19] K. Griest and M. Kamionkowski, *Phys. Rev. Lett.* **64**, 615 (1990).
 - [20] S. Ferrante, M. Perelstein, and B. Yu, Phenomenology of Coherent Freeze-out Mechanism, in preparation.
 - [21] E. W. Kolb and M. S. Turner, *The Early Universe*, Vol. 69 (Taylor and Francis, 2019).
 - [22] H. Goldberg, *Phys. Rev. Lett.* **50**, 1419 (1983), [Erratum: *Phys. Rev. Lett.* 103, 099905 (2009)].
 - [23] M. Quiros, in *ICTP Summer School in High-Energy Physics and Cosmology* (1999) pp. 187–259, [arXiv:hep-ph/9901312](#).



The story of “WIMP meets ALP”